Enhanced method for determining the optical response of highly complex biological photonic structures

Andrés E. Dolinko[1,2,*] and Diana C. Skigin[2]

[1]*Departamento de Biodiversidad y Biología Experimental, Facultad de Ciencias Exactas y Naturales, Universidad de Buenos Aires, Ciudad Universitaria, Pabellón II, C1428EHA Buenos Aires, Argentina*
[2]*Grupo de Electromagnetismo Aplicado, Departamento de Física, Facultad de Ciencias Exactas y Naturales, Universidad de Buenos Aires, and IFIBA–CONICET, Ciudad Universitaria, Pabellón I, C1428EHA Buenos Aires, Argentina*
**Corresponding author: adolinko@df.uba.ar*

Received March 22, 2013; revised July 1, 2013; accepted July 12, 2013;
posted July 12, 2013 (Doc. ID 187657); published August 6, 2013

We present a set of techniques that enhances a previously developed time domain simulation of wave propagation and allows the study of the optical response of a broad range of dielectric photonic structures. This method is particularly suitable for dealing with complex biological structures, especially due to the simple and intuitive way of defining the setup and the photonic structure to be simulated, which can be done via a digital image of the structure. The presented techniques include a direction filter that permits the decoupling of waves traveling simultaneously in different directions, a dynamic differential absorber to cancel the waves reflected at the edges of the simulation space, and a multifrequency excitation scheme. We also show how the simulation can be adapted to apply a near to far field method in order to evaluate the resulting wavefield outside the simulation domain. We validate these techniques, and, as an example, we apply the method to the complex structure of a microorganism called *Diachea leucopoda*, which exhibits a multicolor iridescent appearance.

OCIS codes: (050.1755) Computational electromagnetic methods; (350.4238) Nanophotonics and photonic crystals; (050.6624) Subwavelength structures; (170.1420) Biology.
http://dx.doi.org/10.1364/JOSAA.30.001746

1. INTRODUCTION

The study of the optical response of structures with typical sizes of the order of the optical wavelengths has gained great interest in recent years. Emerging technologies had resulted from the study of photonic materials, which consist of a regular distribution of particles within a host matrix. Depending on the size of the inclusions relative to the operating wavelength, photonic materials can be designed to control the effective electric permittivity and magnetic permeability in order to obtain a specific response (metamaterials), with the possibility of generating a negative refraction index [1] and a great variety of promising applications such as superlensing and optical cloaking [2–6]. On the other hand, all-dielectric photonic crystals exhibit interesting properties that arise from the resonant scattering generated by the specific modulation of the refraction index [7–9]. Also, the photonic band gaps [10] can be designed for specific purposes such as optical switches, Bragg filters, or photonic crystal fibers [11–13].

Another growing research field based on dielectric photonic structures is the study of natural structural color, which is responsible for the iridescent appearance exhibited by a broad diversity of animals and plants [14–16]. Structural color is produced by the selective reflection of light incident on the microscopic structures present in the cover tissues of biological organisms. Optical mechanisms such as interference, diffraction, and scattering are involved to achieve colorful patterns or metallic appearance. These colors usually appear considerably brighter than those of pigments, although they often result from completely transparent materials [17,18]. Unlike artificial photonic materials, the geometry and distribution of these natural media is usually extremely complex, and the simulation of their electromagnetic response requires versatile and accurate tools. The study of this phenomenon contributes to the understanding of different behavioral functions of living species such as thermoregulation and camouflage and, at the same time, inspires new developments of artificial devices.

A large variety of rigorous electromagnetic methods for the calculation of the optical response of a given photonic structure are available, such as the modal method [19–21], the coupled-wave method [22], coordinate-transformation methods [23,24], and the integral method [25–27]. These approaches are very efficient for the accurate determination of the optical response of corrugated interfaces and periodic gratings of canonical shapes. However, in most cases, they are not suitable for dealing with highly complex structures. Another way of studying the electromagnetic response of complex nanostructures is by means of computer simulations. Among them, a widespread approach is the finite-difference time-domain method (FDTD) introduced by Taflove and Hagness around 40 years ago [28], which is based on the Yee algorithm [29] and consists of numerically solving six coupled vector equations obtained from Maxwell's equations in the time domain. The FDTD is a very powerful method and has been improved over the last decades to account for a great variety of problems in electrodynamics. Recently, Kolle *et al.* implemented an interface for the MEEP package (an FDTD implementation) [30], which permits introducing the profile of the diffracting structure via binary images based on refraction index contrasts in scanning electron microscope or

transmission electron microscope (TEM) images [31]. However, it is heavily time consuming, and requires large computer resources and even parallelization for very large simulation spaces [32].

In this paper, we present a set of processing techniques that improve the performance of the simulation method presented in [33], which allows studying the propagation of electromagnetic waves in a dielectric medium of arbitrary refraction index distribution. Within the simulation, the evolution of the propagating waves can be easily visualized on a conventional computer during runtime. One of the highlights of the proposed method is its versatility to obtain the optical response of an arbitrary dielectric photonic structure. The refraction index distribution can be artificially generated using any available computational design tool for digital image edition, or it can be obtained from a digitized electron microscope image of a real physical sample. The presented tools complement and enhance the former implementation of the method in several aspects.

In Section 2, we summarize the basic concepts of the simulation. In Sections 3–6, we present a set of techniques which permit us to control and analyze the behavior of the waves within the simulation: (i) a direction filter (DF) that permits us to decouple waves traveling simultaneously in different directions and also allows us to determine the field of energy flux in any type of wave (Section 3); (ii) an active system to cancel waves reflected at the edges of the simulation space, which allows the simulation of boundary conditions that represent an unbounded virtual space (Section 4); and (iii) a multifrequency excitation scheme which increases the computing speed since it avoids sequential frequency sweeps to obtain the spectral response of a given structure (Section 5). Finally, in Section 6, we show how to obtain the far field (outside the simulation space) from the near field. As an example, in Section 7 we apply the simulation method, including the whole set of developed techniques, to obtain the optical response of the photonic structure present in the tissue of a microorganism. Concluding remarks are given in Section 8.

2. DESCRIPTION OF THE SIMULATION

The basic idea underlying the whole method is the parallelism between electromagnetic and mechanical waves, as already reported in the literature [34]. It proposes the use of the computer as a generator of a virtual environment where the physical differential law is used to make the system evolve along the time, as it would evolve in the real physical world.

The simulation reproduces the propagation of transverse mechanical waves along the time. Although the details can be found in [33], for the sake of completeness, we describe the physical model and introduce the parameters that are used in the following sections.

The physical model consists of a two-dimensional array of $p \times q$ particles of mass m contained in the x–y plane. Each particle is joined to its four nearest neighbors by means of elastic springs of elastic constant k and separated by a distance d. The movement of the particles is constrained to the z axis, which is normal to the plane of the two-dimensional array along which the waves propagate, as shown in Fig. 1. The net force on each particle is null when it is located at $z = 0$. A wave is generated by applying an external force along the z axis to certain particles, depending on the type of excitation.

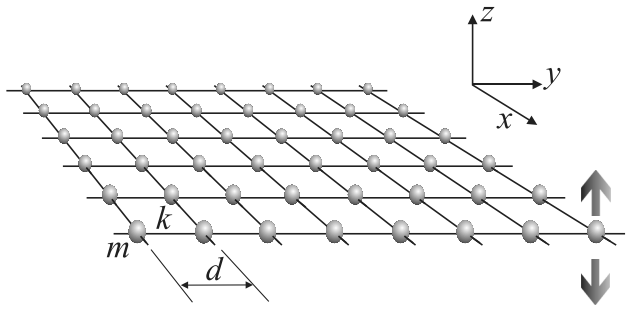

Fig. 1. Particle array representing the physical model of the simulation.

For large p and q, the array of particles can be considered as a continuous medium representing a tensioned elastic membrane. The time evolution of the system is described by the following wave equation:

$$\frac{\partial^2 A}{\partial t^2} = \frac{T}{\mu}\nabla^2 A - \frac{\gamma}{\mu}\frac{\partial A}{\partial t} + \frac{E_t}{\mu}, \tag{1}$$

where $A = A(x, y, t)$ is the position along the z axis of a differential element of the membrane, T is the tension of the membrane, $\gamma = \gamma(x, y)$ is a damping constant, $\mu = \mu(x, y)$ is the surface mass density, and $E_t = E_t(x, y)$ is the time-varying applied external force. $v = \sqrt{T/\mu}$ represents the speed of the waves. Equation (1) is discretized in space and time and its dynamic evolution is obtained by means of an iterative algorithm [33].

Making an analogy with optics, regions with mass density μ_0 can be identified with vacuum, i.e., a medium of refraction index $n_0 = 1$, while a region with an arbitrary mass density μ corresponds to a medium with a real part of the refraction index $n = \sqrt{\mu/\mu_0}$. This approach permits optical phenomena involving dielectric materials illuminated by transverse electric (TE) polarized light to be reproduced in two-dimensional configurations.

One of the advantageous features of this method is the possibility of defining the simulation domain by means of digital images or bitmaps. Each pixel in the image represents the position of the particle in the array. In this manner, a digital image of $p \times q$ pixels automatically defines the size of the simulation domain. An appropriate constant σ_p given in units of [nm/pixel] links the size of an object in the digital image, in pixels, with the actual physical size of the sample to be simulated, which is usually measured in nanometers.

Three bitmaps of equal size are defined within the simulation code to introduce different characteristics of the structure and the illumination conditions, which are denoted as M (mass density), D (damping), and E (excitation). The gray levels in the M bitmap represent the mass distribution within the array, which should be assigned using an adequate linear conversion function. Bitmap D encodes the damping constant of each point of the array, which allows introducing attenuation in the medium, and bitmap E is introduced to specify the excitation, i.e., the particles on which the external force is applied. Following the analogy with the propagation of electromagnetic waves in an optical medium, the M bitmap determines the refraction index distribution, bitmap D

specifies the regions where there is absorption, and bitmap E specifies the location and shape of light sources. The gray level matrices M, D, and E are related to the matrices M_{phys}, D_{phys}, and E_{phys}, respectively, which contain the values of mass, damping, and excitation measured in physical units, by

$$M_{\text{phys}} = m_0 + M m_p, \tag{2}$$

$$D_{\text{phys}} = D\mu_p, \tag{3}$$

$$E_{\text{phys}} = r_p(E - 128), \tag{4}$$

where m_0 is the minimum mass value, which is associated with the refraction index of vacuum. The proportionality constant m_p in Eq. (2) has units of [kg/gl] and the constant μ_p has units of $[(\text{N} * \text{s})/(\text{m} * \text{gl})]$ ([gl] is the gray level unit within a scale of 0–255 in which the digital images are represented). r_p in Eq. (4) is a constant of units [N/gl], which transforms the value of gray level provided by the bitmap E to a value of force. In Eq. (4), a value $E = 128$ indicates that no force is applied on the particle. Then, values over 128 are interpreted as positive forces and gray level values under 128 are interpreted as negative forces. The harmonic excitation is introduced by means of the time-varying applied external force as

$$E_t = E_{\text{phys}} \sin(\omega \tau_n n_c + \varphi), \tag{5}$$

where ω is the angular frequency of the excitation, φ is the initial phase, and τ_n is a time-adapting constant in units of [s/cycle] that converts the integer number of iteration cycles n_c into a physical time variable. The product $\tau_n n_c$ represents the discretized time variable, and the product $\omega_d = \omega \tau_n$ in Eq. (5) can be regarded as a digitized angular frequency measured in [rad/cycle].

The Nyquist–Shannon sampling theorem [35] states that the frequency of the signal sampling must be at least twice the highest frequency component of the signal in order to preserve the alternating nature of the external excitation after the sampling. In our case, the sinusoidal waveform of the externally applied force has a period 2π, and then it should be sampled at minimum at twice its frequency, that is, every π radians or less every iteration cycle. This implies that ω_d should be smaller than π rad/cycle. On the other hand, the adapting constants τ_n and σ_p are related by

$$\tau_n = \frac{v_d}{v_{\text{phys}}} \sigma_p, \tag{6}$$

where v_d is the digitized speed of the waves (measured in [pixels/cycle]) and v_{phys} is the physical speed of the waves measured in [nm/s]. In the case of optical waves in vacuum, $v_{\text{phys}} = v_0$ corresponds to $c = 2.99792 \times 10^{17}$ nm/s. Therefore, the digitized angular frequency ω_d can be expressed as

$$\omega_d = \omega \frac{v_d \sigma_p}{c}. \tag{7}$$

The above expression implies that once the optical frequency is fixed, the Nyquist–Shannon criterion requires

$$v_d \sigma_p < \frac{\pi c}{\omega}. \tag{8}$$

On the other hand, the Courant–Friedrichs–Lewy condition [36] imposes that v_{d0}, the digital counterpart of the maximum speed $v_0 = c$, must satisfy $v_{d0} \leq 1$ pixel/cycle. That is, the maximum allowed digitized wave speed that guarantees the stability of the simulation is one pixel per cycle of iteration. A speed beyond this value would cause the simulation to diverge. In other words, the dynamical information can be transferred to a maximum distance of one pixel, i.e., from one pixel to the next one, in each iteration cycle.

3. DIRECTION FILTER

We propose a simple and natural DF to isolate a single wave traveling in a given direction. This method is based on a wave subtraction technique, and it works automatically for any wavelength, amplitude, direction, waveform, and also in the presence of other waves traveling in different directions.

For the sake of clarity, in the following subsection we describe the DF formulation for one-dimensional problems and in Subsection 3.B we generalize it to two dimensions.

A. Mathematical Formulation of the DF in One Dimension

For a given time-evolving function $A(x,t)$, we propose the operator

$$\mathcal{F}^{(+)}[A(x,t)] = A(x, t + \Delta t) - A(x - v\Delta t, t), \tag{9}$$

where v is a constant representing a speed. If and only if $A(x,t)$ represents a wave traveling at speed v toward the $+x$ direction, it must satisfy

$$A(x, t + \Delta t) = A(x - v\Delta t, t). \tag{10}$$

Substituting Eq. (10) in Eq. (9), we obtain

$$\mathcal{F}^{(+)}[A(x,t)] = A(x - v\Delta t, t) - A(x - v\Delta t, t) = 0 \quad \forall\, t. \tag{11}$$

The positive DF operator $\mathcal{F}^{(+)}$ cancels waves traveling toward the $+x$ direction. Correspondingly, $\mathcal{F}^{(-)} = A(x, t + \Delta t) - A(x + v\Delta t, t)$ is the negative DF operator, and it cancels waves traveling toward the $-x$ direction. In other words, the DF operator cancels a wave $A(x,t)$ traveling in a given direction by subtracting from it the same wave but evaluated in a previous instance and in a position displaced by an amount $\Delta x = v\Delta t$ from its present position. This is schematically shown in Fig. 2.

Let us now evaluate the effect of the positive DF operator in a more general case (the analysis for the negative DF operator is completely analogous). Suppose that $A(x,t) = B^+(x,t) + B^-(x,t)$ is the superposition of two waves of arbitrary shapes traveling with speed v toward opposite directions $+x$ and $-x$, respectively. Taking into account that

$$A(x - v\Delta t, t) = B^+(x - v\Delta t, t) + B^-(x - v\Delta t, t) \tag{12}$$

and

$$A(x, t + \Delta t) = B^+(x, t + \Delta t) + B^-(x, t + \Delta t), \tag{13}$$

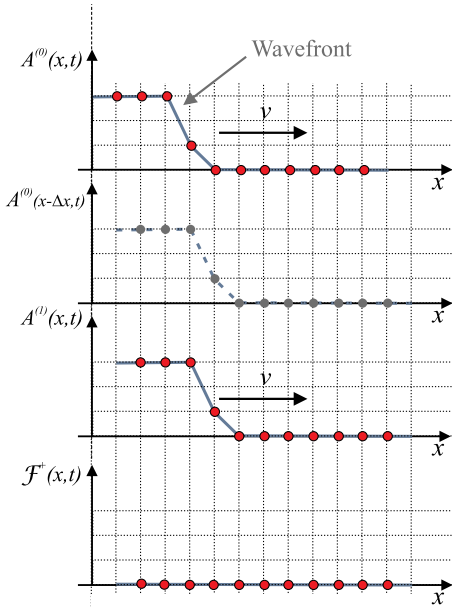

Fig. 2. Geometric representation of the action performed by the positive DF operator.

by applying $\mathcal{F}^{(+)}$ to this new function, we get

$$\mathcal{F}^{(+)}[A(x,t)] = B^+(x,t+\Delta t) + B^-(x,t+\Delta t) - B^+(x-v\Delta t,t) - B^-(x-v\Delta t,t). \quad (14)$$

Since $B^+(x,t)$ and $B^-(x,t)$ are waves traveling toward the $+x$ and $-x$ directions, respectively, they satisfy

$$B^+(x,t+\Delta t) = B^+(x-v\Delta t,t) \quad (15)$$

and

$$B^-(x,t+\Delta t) = B^-(x+v\Delta t,t). \quad (16)$$

Therefore,

$$\mathcal{F}^{(+)}[A(x,t)] = B^-(x+v\Delta t,t) - B^-(x-v\Delta t,t). \quad (17)$$

As expected, $B^+(x,t)$ is completely cancelled. By calling $x' = x + v\Delta t$, Eq. (17) can be rewritten as

$$\mathcal{F}^{(+)}[A(x'-v\Delta t,t)] = B^-(x',t) - B^-(x',t-2\Delta t), \quad (18)$$

which represents a wave traveling toward the $-x$ direction. By dividing both sides of Eq. (18) by $2\Delta t$ and taking the limit $\Delta t \to 0$, Eq. (18) is reduced to

$$\mathcal{F}^{(+)}[A(x,t)] \approx 2\Delta t \frac{\partial B^-(x+v\Delta t,t)}{\partial t}. \quad (19)$$

Expression (19) reveals the effect of the DF operator on a wave of general shape traveling in a nonfiltered direction. For small Δt compared with the time period of the higher harmonic component of $B^-(x,t)$, the filtered wave is proportional to the time derivative of the original wave.

B. Generalization of the DF to Two Dimensions

Consider a two-dimensional scalar wavefield $A_2(\mathbf{r},t)$. The expression for the DF operator (9) in $\mathbb{R}^2$ is

$$\mathcal{F}_2^{(\mathbf{v},\delta)}[A_2(\mathbf{r},t)] = A_2(\mathbf{r},t+\delta) - A_2(\mathbf{r}-\mathbf{v}\delta,t). \quad (20)$$

This operator filters waves traveling with phase speed $|\mathbf{v}|$ in the direction of $\mathbf{v}$, with a characteristic time delay $\delta = \Delta t$ (bold letters represent vectors). To find out the effect produced by the DF operator on waves traveling in directions different from the filtering direction determined by $\mathbf{v}$, we consider a two-dimensional plane wave

$$A_2(\mathbf{r},t) = Ae^{i\mathbf{k}_w(\mathbf{r}-\mathbf{v}_w t)}, \quad (21)$$

where $\mathbf{k}_w$ is the wave-vector, $\mathbf{v}_w = \omega/|\mathbf{k}_w|\mathbf{k}_w$ is the velocity of the wave, and ω is its angular frequency. Substitution of Eq. (21) into Eq. (20) yields

$$|\mathcal{F}_2^{(\mathbf{v},\delta)}(\alpha)| = A|e^{-i\omega\delta} - e^{-i\omega\delta\cos(\alpha)}|, \quad (22)$$

where $|\mathcal{F}_2^{(\mathbf{v},\delta)}(\alpha)|$ is the complex amplitude of the filtered wave and α is the angle between the propagation direction ($\mathbf{k}_w$) and the filtering direction ($\mathbf{v}$) (see Fig. 3).

To quantify the performance of the DF, we define the relative attenuation μ_a of the wave as

$$\mu_a(\alpha) = 1 - |\mathcal{F}_2^{(\mathbf{v},\delta)}(\alpha)|/|\mathcal{F}_2^{(\mathbf{v},\delta)}|^{\max}, \quad (23)$$

where $|\mathcal{F}_2^{(\mathbf{v},\delta)}|^{\max}$ stands for the maximum value of $|\mathcal{F}_2^{(\mathbf{v},\delta)}(\alpha)|$ for $\alpha \in [0°, 360°]$. As mentioned at the end of Subsection 3.A, the requirement for the DF to work properly is that δ must be small compared to the time period of the highest harmonic component of $A_2(\mathbf{r},t)$. Therefore, it can be easily proved that in the limit $\delta \to 0$, the attenuation (23) takes the simple form

$$\mu_a(\alpha) = \frac{1}{2}[\cos(\alpha) + 1]. \quad (24)$$

Figure 4 shows the relative attenuation of a plane wave as a function of α. As expected, the maximum attenuation is obtained for $\alpha = 0$, that is, when the propagation direction of the plane wave coincides with the filtering direction.

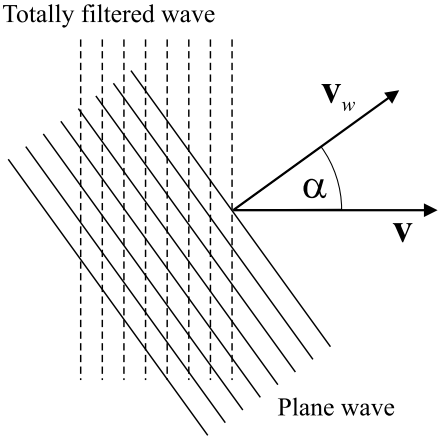

Fig. 3. Angle α between the direction of propagation of the plane wave (along $\mathbf{v}_w$) and the filtering direction (along $\mathbf{v}$).

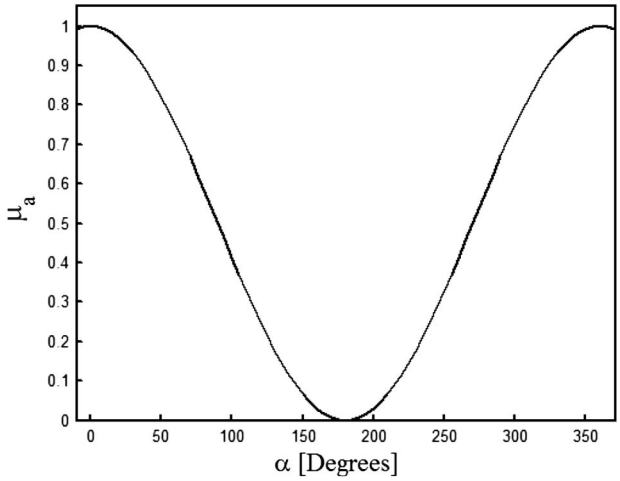

Fig. 4. Attenuation of the plane wave as a function of the angle α between its direction of propagation and the filtering direction.

Conversely, the attenuation is minimum for the wave traveling in the opposite direction, that is, for $\alpha = 180°$. In Fig. 5, we show the performance of the DF for a circular wavefront, which can be regarded as a superposition of plane waves propagating along all possible directions. The amplitude of the obtained filtered wave is shown in gray levels.

C. Numerical Considerations

As presented above, the DF is characterized by two parameters: $\mathbf{v}$, which determines the speed and direction of the wave to be filtered, and δ, the characteristic delay. However, as in any digital simulation, the space–time domain is discretized, and this discretization imposes certain constrains on the DF parameters.

From Eq. (20), it becomes evident that the filtering operation will be effective if the spatially displaced wavefield $A_2(\mathbf{r} - \mathbf{v}\delta, t)$ has exactly the same shape as $A_2(\mathbf{r}, t + \delta)$. Since in the discretized domain the minimum separation distance is 1 pixel and the simulation allows a maximum digitized wave speed $v_{d0} \leq 1$ pixel/cycle (according to the Courant–Friedrichs–Lewy condition), the traveling wave advances a distance $d_0 = |\mathbf{v}|t = v_{d0} \times \Delta n_c \leq 1$ pixel in one iteration cycle ($\Delta n_c = 1$), and therefore $A_2(\mathbf{r}, t + \delta)$ will have the same shape as $A_2(\mathbf{r} - \mathbf{v}\delta, t)$ exactly after $1/v_{d0}$ iteration cycles, with $(1/v_{d0}) \in \mathbb{Z}$. During intermediate iteration steps, the wave will take interpolated values between $A_2(\mathbf{r} - \mathbf{v}\delta, t)$ and $A_2(\mathbf{r}, t + \delta)$ that will not exactly match the shape of either of them. According to this, the necessary requirement for a good performance of the DF within the simulation is that the speed of the waves must be set to $v_{d0} = 1$ pixel/Δn_c, with $\Delta n_c \in \mathbb{Z}$ being the integer number of iteration cycles in which the wave advances a distance of exactly 1 pixel. Therefore, the characteristic delay of the filter must be $\delta = \Delta n_c = 1$ pixel/v_{d0} for a spatial shifting of $A_2(\mathbf{r} - \mathbf{v}\delta, t)$ equal to 1 pixel. In our simulations, we usually set the second allowed digitized speed $v_{d0} = 0.5$ pixels/cycle, (i.e., $\Delta n_c = 2$). Therefore, in this case, $\delta = 2$ cycles for a spatial shifting of 1 pixel in $A_2(\mathbf{r} - \mathbf{v}\delta, t)$. Although we could eventually use spatial shiftings larger than 1 pixel, larger shiftings lead to larger values of the characteristic delay δ, during which the shapes of $A_2(\mathbf{r} - \mathbf{v}\delta, t)$ and $A_2(\mathbf{r}, t + \delta)$ would be more affected by the numerical errors, thus decreasing the quality of the directional filtering.

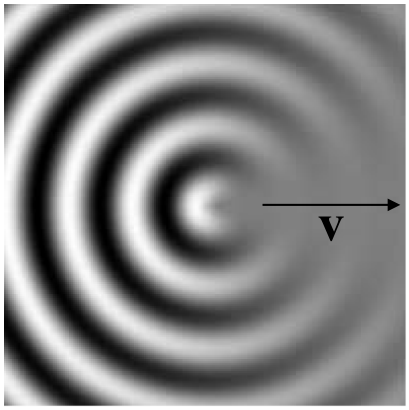

Fig. 5. Angular effect of the DF on a circular wavefront.

It is worthwhile mentioning that the above conditions are valid for the implementation of the DF in the orthogonal directions x and y, which coincide with the rows and columns of the discretized array of particles comprising the simulation medium, as shown in Fig. 1. In the present paper we use four DFs corresponding to the directions $+x$, $-x$, $+y$, and $-y$. From a practical programming point of view, the DF is applied to the waves evolving in the two-dimensional array defined by the simulation, called main plane. However, the resulting directionally filtered waves are stored in secondary planes. These secondary planes show time-evolving waves that are filtered images of the waves evolving in the main plane, and therefore the DF does not affect the physics of the system. In this case, we have four secondary planes that store the filtered waves traveling in the $+x$, $-x$, $+y$, and $-y$ directions, respectively.

To illustrate the behavior of the DF, in Fig. 6(a) we show the main plane of the simulation of a linear source emitting Gaussian waves in directions $\pm x$. Figures 6(b) and 6(c) show the secondary planes that contain the wavefield of Fig. 6(a) after the application of the DF that cancels waves traveling toward the $+x$ and the $-x$ direction, respectively.

One of the main applications of the DF is the method for evaluating the energy flux of any simulated wavefield. This method makes use of the waves filtered in the orthogonal directions $\pm x$ and $\pm y$. Let us call I_{x+}, I_{x-}, I_{y+}, and I_{y-} the intensity (calculated as the time integration of the squared amplitude) of the waves traveling toward the $+x$, $-x$, $+y$, and $-y$ directions, respectively. Then, the quantities $\phi_x = I_{x+} - I_{x-}$ and $\phi_y = I_{y+} - I_{y-}$ are proportional to the energy flux along the x and y directions, respectively. Consequently, the vector field $\mathbf{F}$ defined as

$$\mathbf{F} = (\phi_x, \phi_y) \tag{25}$$

is proportional to the energy flux vector field.

It should be mentioned that the DF developed here could also be applied to experimental data. For instance, the method of Fourier transform profilometry presented in [37] permits digitalizing the evolution of surface water waves along time. Therefore, the technique proposed in this paper also enables the calculation of the energy flux field for real systems.

4. DYNAMIC DIFFERENTIAL ABSORBER

It is well known that any computer wave simulation can only reproduce the propagation of waves in a finite domain.

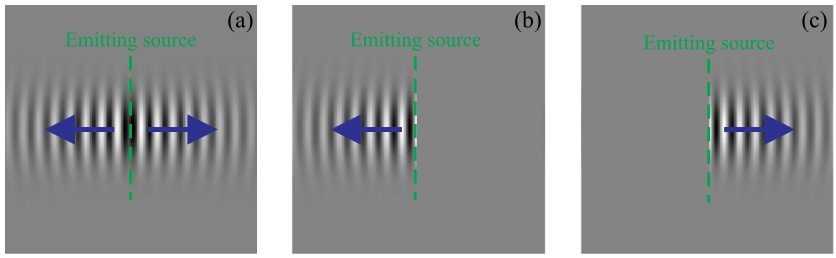

Fig. 6. (a) Source emitting Gaussian waves in directions $+x$ and $-x$. (b) Secondary plane of the DF that cancels waves traveling toward the $+x$ direction. (c) Secondary plane of the DF that cancels waves traveling toward the $-x$ direction. Arrows show the wavefront propagation directions.

However, the waves that arrive at the edges of the simulation domain are naturally reflected back [33]. Therefore, in order to simulate open boundaries, it is necessary to artificially cancel these reflected waves. Several methods have been proposed for this purpose [33,38–41], each of them having its advantages and disadvantages. One possibility to avoid these reflections is to place a slab of an absorbing medium adjacent to the edges of the domain. In its basic implementation, this approach reduces the reflected waves, but it does not completely cancel them [33]. Besides, the absorbing region produces an unnecessary increment of the size of the simulation space and, consequently, the computation time also increases.

A highly improved version of the procedure described above is the so called *perfectly matched layer* (PML) [28,38]. This method is the most widespread technique to cancel reflected waves in electromagnetic simulations, and it consists of introducing an absorbing anisotropic layer at the edges of the simulation space. Within this layer, the differential wave equation is modified by including a special transformation that produces a rapid attenuation of the wave as it propagates. Although this method is very efficient, it requires a layer of finite thickness to allow the decay of the waves. Besides, waves traveling parallel to the layer are not attenuated by the PML method, producing the accumulation of nonrealistic energy in that region.

In this section, we present an alternative approach to simulate the open space by cancelling reflected waves at the edges of the simulation domain. The method, called dynamic differential absorber (DDA), is based on an intuitive concept and its main advantage is that it does not require a layer of a given thickness to cancel the waves, i.e., it produces the absorption of the wave within a layer of infinitesimal thickness, and this saves computation space and time. On top of that, the method automatically cancels waves of any amplitude, shape, or frequency with the same efficiency, and this constitutes a great advantage that enables the use of multifrequency excitation, as shown in Section 5.

The basic idea behind the DDA is similar to the analytic boundary condition of the differential wave equation proposed several decades ago by Engquist and Majda [39] first, and by Higdon [40,41] later. The framework of their formulations is the so-called space-time extrapolation, which basically presents a static view of the problem. The approach by Engquist and Majda [39] consists of finding an analytic boundary condition that is later discretized, whereas the method by Higdon [40,41] directly works with the finite difference approximation of the differential wave equation. Although our approach is closer to the latter method, it differs from Higdon's work especially in the case of oblique incidence. In this case, Higdon's method finds the range of angles for which the best absorption is obtained, but it does not provide a solution to improve the absorption for an arbitrary angle of incidence. The novelty of the DDA is that it actively adapts the absorbing performance by detecting the angle of incidence of the waves reaching the absorber, which greatly improves the absorbance. Additionally, our DDA is based on an intuitive and simple idea, which provides more physical insight to the problem.

In the following subsection we present the basic formulation of the DDA for the 1D case, called simple dynamic differential absorber (SDDA), and then we develop the adaptive dynamic differential absorber (ADDA), which is a generalization to two and more dimensions.

A. Simple Dynamic Differential Absorber

Let us examine the movement of a wave propagating along the x axis toward the $+x$ direction, at two fixed points $x = x_a$ and $x = x_b$, as shown by the dots in Fig. 7. As the wave passes through, the amplitude A_b at x_b will take the value of A_a at x_a after a time delay given by $\Delta t = \Delta d/v_w$, where $\Delta d = x_b - x_a$ and v_w is the phase velocity of the wave (within this context, the term "amplitude" refers to the magnitude of the wavefield at a given point).

The key idea underlying the DDA is the following: if we artificially control the amplitude A_b of the wave at x_b and make it move in such a way that A_b copies the amplitude A_a with the right time delay, the behavior of the propagating wave for $x < x_b$ will not be affected as it passes through. In fact, if x_b is a point located at the edge of the simulation domain, the incoming wave will not be affected at this point and it would continue propagating as if there were no boundary. Therefore, the SDDA consists in controlling the movement of a point located at x_b, called the absorbing point, according to the behavior of the incoming wave at x_a, called the reading point. Mathematically, this can be expressed as

$$A_b^{(t_1)} = A_a^{(t_0)}, \tag{26}$$

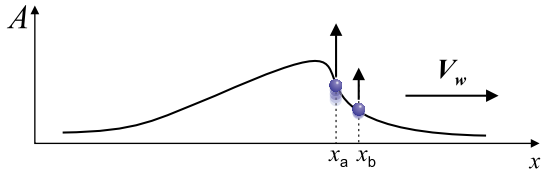

Fig. 7. Amplitude of a propagating wave at two fixed points located in $x = x_a$ and $x = x_b$.

where $A_b^{(t_1)}$ is the amplitude of the wave at x_b in a certain instant t_1 and $A_a^{(t_0)}$ is the amplitude of the wave at x_a in a previous instant$t_0 = t_1 - \Delta t$, with $\Delta t = \delta_d \Delta d$. In this context, $\delta_d = 1/v_w$ is the *differential delay* which depends on the medium characteristics via the phase velocity of the waves within the propagating medium.

Although the above equations do not condition the distance between the absorbing and the reading points, within the simulation method the discretized nature of the space–time domain must be taken into account, as already explained in Subsection 3.C for the DF. Since the minimum distance between the reading and the absorbing points is of one pixel, we also set the allowed digitized wave speed $v_{d0} = 0.5$ pixels/cycle (see Subsection 3.C), and then $\delta_d = 1/v_{d0} = 2$ iteration cycles. If, for instance, a 1D simulation space is M pixels long, the rightmost pixel $m = M$ is forced to move as

$$A_M^{(n_c)} = A_{M-1}^{(n_c-2)}, \tag{27}$$

where $A_{M-1}^{(n_c-2)}$ is the amplitude of the wave at the pixel $M-1$ stored two iteration cycles before the present cycle n_c. Similarly, the leftmost pixel $m' = 1$ is forced to move as

$$A_1^{(n_c)} = A_2^{(n_c-2)}, \tag{28}$$

where $A_2^{(n_c-2)}$ is the amplitude of the second pixel stored two iteration cycles before the present cycle n_c.

B. Adaptive Dynamic Differential Absorber

If the simulation domain is two-dimensional, the SDDA presented in the previous subsection would only be effective for waves propagating normally to the edge of the simulation space (or whose wavefronts are parallel to the edges of the domain). In order to develop a direction-sensitive method that could properly absorb waves propagating in different directions, small corrections must be introduced into the differential delay used to cancel the incoming waves.

The effective wavelength λ_{eff} of the wave that arrives at the edge of the simulation space is given by

$$\lambda_{\text{eff}} = \lambda_w / \cos(\alpha), \tag{29}$$

where λ_w is the actual wavelength of the incoming wave and α is the angle between the direction of propagation and the normal to the edge of the simulation space. Then, the effective phase velocity v_{eff}, the phase velocity of the wave along the direction normal to the edge of the simulation space, depends on the angle of incidence and is given by

$$v_{\text{eff}} = \frac{\omega}{k_{\text{eff}}} = \lambda_{\text{eff}} f \tag{30}$$

with $\omega = 2\pi f$, k_{eff} being the effective wavenumber and f the frequency of the wave. This is schematically shown in Fig. 8. Consequently, the effective differential delay δ_{eff} becomes

$$\delta_{\text{eff}} = \frac{1}{v_{\text{eff}}} = \frac{\cos(\alpha)}{v_w} = \delta_d \cos(\alpha), \tag{31}$$

which implies that δ_{eff} is always smaller than δ_d.

To determine δ_{eff}, the reading point must provide information not only about the time-varying amplitude of the wave to be cancelled, but also about its direction of propagation, given by α. This angle can be obtained by evaluating the energy flux vector at the reading point, using the method described in Subsection 3.C. For example, for the right-hand side edge of the simulation space, α is given by

$$\alpha = \arctan\left(\frac{\phi_y}{\phi_x}\right). \tag{32}$$

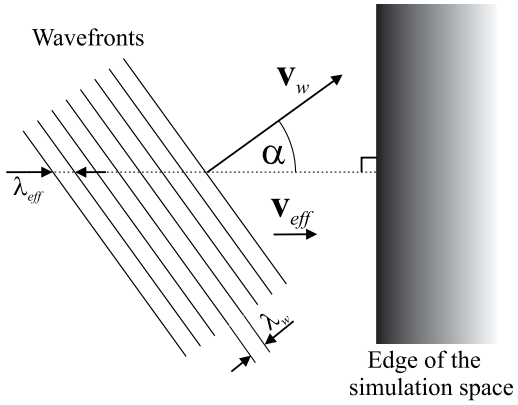

Fig. 8. Effective wavelength λ_{eff} and effective phase velocity v_{eff} of an obliquely incident wave forming an angle α with the normal to the simulation space edge.

In practice, to clearly establish the direction of the incoming wave before it is affected by the edge of the simulation space, the information about the direction of the incoming wave is taken from points located between two and four pixels away from the edge of the simulation space, i.e., from the absorbing points. On the other hand, if the wave speed is set to $v_{d0} = 0.5$ pixels/cycle, δ_{eff} is a real number between 2 and 0 for α between 0° and 90°, respectively. Since the number of cycles δ_{eff} must be an integer, the resulting value Δt must be approximated to the closest integer value. This implies that the allowed discretized delays ($\delta_{\text{eff}} = 2$, 1, and 0) will only match the required delay for three angles of incidence, that in this case are $\alpha = 0°$, 60°, and 90°. Therefore, in order to increase the number of allowed discretized delays, the wave speed can be decreased and set, for instance, to $v_{d0} = 0.1$ pixels/cycle. In this case, δ_{eff} will be bounded between 10 and 0, for α between 0° and 90°, respectively. Then, the number of discretized delays is increased, and the error between the calculated and the allowed integer delays is minimized, as shown in Fig. 9. Increasing the number of discretized delays improves the effectiveness of the ADDA. Then, to increase this number we can either increase the distance between the reading and the absorbing point, or decrease the wave speed v_{d0}. Depending on the requirements of speed and usable space size of the simulation, the best choice should be made. Figure 10 shows the location of the absorbing points (black dashed–dotted line) and the reading points (white dotted line) for a two-dimensional space. The distance Δd (magnified for clarity) between the reading and the absorbing points is also indicated.

Despite the difference between the calculated and the discrete values of δ_d introduced for certain incidence angles by the discretization process, it was verified that these errors do not significantly affect the performance of the ADDA, even for $\delta_d = 2$ (second maximum digitized wave speed allowed) and

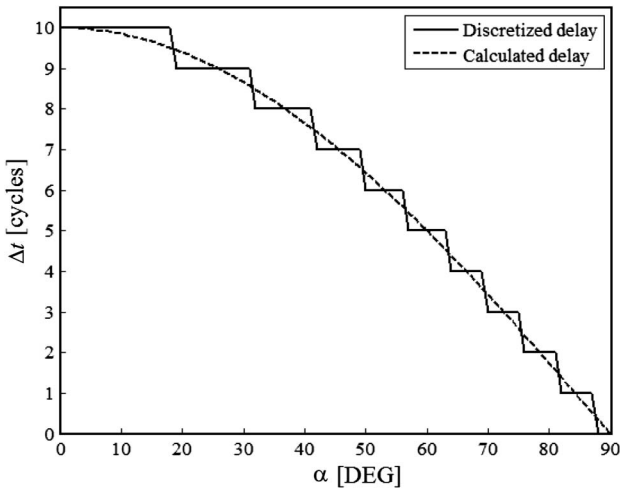

Fig. 9. Delay versus angle of incidence: discretized (solid line) and calculated (dashed line).

$\Delta d = 1$ pixel (maximum available space), as will be shown in the next subsection. Making an analogy with electronics, the proposed method behaves like an active device, which reads an input signal and reacts accordingly to return a post-processed output signal. In this sense, this method is different from most available absorbing methods, which behave like passive devices whose response does not take into account the input signal.

C. Validation

In order to evaluate the performance of the ADDA, the reflectance, defined as the ratio of the reflected to the incident intensity, was calculated for a Gaussian beam incident on the edges of the simulation space with different angles. In all cases, the distance between the reading and the absorbing points was set to $\Delta d = 1$ pixel. Figure 11 shows the reflectance as a function of the angle of incidence for $\delta_d = 2$ (blue solid line), $\delta_d = 4$ (green dashed line), and $\delta_d = 8$ (red dotted line). It can be observed that as δ_d is increased, the overall reflectance decreases, that is, a better

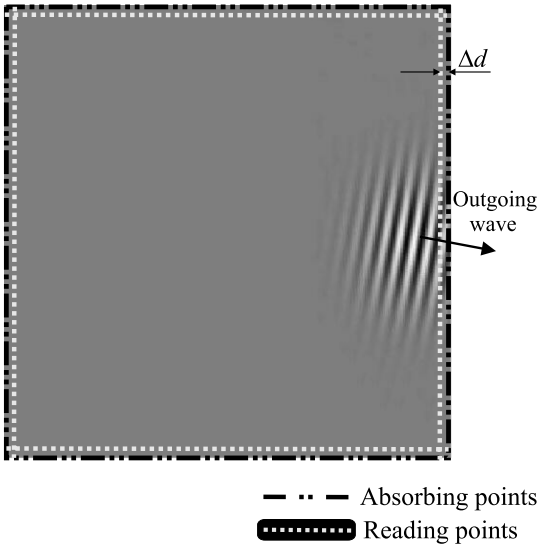

Fig. 10. Location of the absorbing and the reading points for a 2D simulation space. The distance Δd is also indicated.

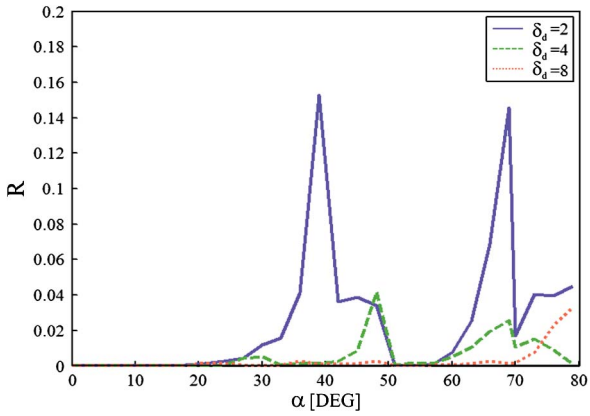

Fig. 11. Numerical experiment with the ADDA: Reflectance versus angle of incidence α for $\delta_d = 2$ (blue solid line), $\delta_d = 4$ (green dashed line), and $\delta_d = 8$ (red dotted line).

performance of the absorber is obtained. For $\delta_d = 2$, there are peaks of relatively high reflectance for 39° and 69°. In the case of $\delta_d = 4$, the reflectance also shows peaks, but less intense than for $\delta_d = 2$. These peaks are located at the angles of incidence for which the difference between the calculated and the available integer delays is maximized. As the number of integer delays is increased (by increasing δ_d), a better matching between the calculated and the available integer delays is obtained (see Fig. 9), and the intensity of the reflectance peaks is gradually reduced, as observed for $\delta_d = 8$ in Fig. 11.

Figure 12 shows the attenuation produced by the ADDA expressed in decibels (dB), and calculated as $\chi = -10\log_{10}(R)$, where R is the reflectance. It can be noticed that for the angles for which the matching between the integer and the calculated delays is better, the attenuation values reach up to 44.2 dB for $\delta_d = 2$, 64.5 dB for $\delta_d = 4$ and 49.4 dB for $\delta_d = 8$. As a reference, the maximum attenuation values obtained with the PML applied within the FDTD method lie between 20 and 39 dB for small incidence angles, depending on the setting parameters of this method [38].

It can also be observed in Fig. 12 that, for angles of incidence greater than approximately 25°, the best (larger) attenuation is obtained for $\delta_d = 8$, whereas for small angles of incidence the attenuation obtained for $\delta_d = 4$ is better. This result can be explained by taking into account that smaller angles of incidence require higher values of the effective

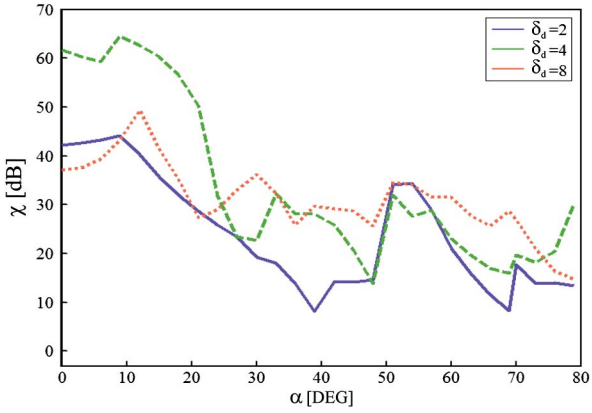

Fig. 12. Attenuation versus angle of incidence α for $\delta_d = 2$ (blue solid line), $\delta_d = 4$ (green dashed line), and $\delta_d = 8$ (red dotted line).

differential delay δ_{eff}, as determined by Eq. (31). In this case, there are more iteration cycles between the reading and the absorbing instants for $\delta_d = 8$ than for $\delta_d = 4$. Then, if the sampling frequency of the shortest wavelength involved is low, a wave that propagates a fraction of pixel will be represented in the next iteration cycle by a natural interpolation produced by the simulation. When the wave advances one pixel, the accumulated numerical errors produced by interpolation will be more in the case of $\delta_d = 8$ than in the case of $\delta_d = 4$, producing a higher mismatch between the read waveform and the waveform that actually reaches the absorbing point. This produces a better performance for $\delta_d = 4$ for small angles of incidence. Therefore, in order to reduce the interpolation errors and improve the absorbing characteristics for small incidence angles, i.e., for high differential delays δ_d, the sampling frequency must be increased, and this is done by decreasing the constant σ_p as described in Section 2.

As can be noticed, the angles considered in Figs. 11 and 12 range from 0° to 80° due to the technical difficulties to evaluate the reflectivity for grazing angles near (and at) 90°, with the simulation. This limitation arises mainly from the requirement of a minimum width of the Gaussian beam in order to approximately represent a highly directional incident plane wave. For grazing angles, a very wide simulation space is required, which increases as α approaches 90°. Therefore, the response of the absorber for the range of angles comprehended in the interval (80°,90°] was directly evaluated by checking the values of the effective differential delay, which are automatically set by the absorber during runtime. It was verified that the obtained values for the discretized δ_{eff} were in good agreement with those obtained theoretically by means of Eq. (31) for the corresponding angles.

The effect of the ADDA is graphically shown in Fig. 13 for an incident Gaussian beam forming an angle of 20° with the normal to the edge of the simulation space. Figure 13(a) shows the intensity diagram without the ADDA, where the reflected wave can be observed, and Fig. 13(b) shows that the reflected beam is almost completely cancelled when the absorber is activated.

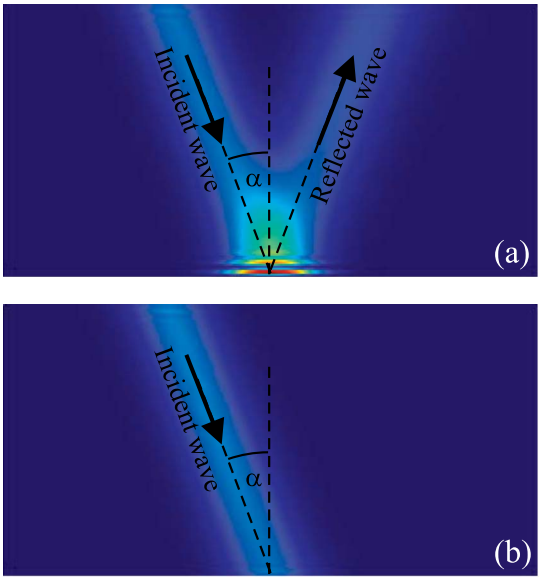

Fig. 13. Intensity diagram of a Gaussian beam forming an angle $\alpha = 20°$ with the normal to the lower horizontal edge of the simulation space for the case $\delta_d = 4$. (a) Without ADDA and (b) with ADDA.

It is worthwhile mentioning that the DDA is a general method that could be applied to waves of any nature, i.e., mechanical, electromagnetic, and potentially even to quantum waves governed by Schrodinger's equation.

5. MULTIFREQUENCY EXCITATION AND TUNING FILTER

The optical response of a structure is usually described by its reflectance and transmittance as a function of the wavelength. To evaluate the optical response in a more efficient manner, in this section we introduce a multifrequency excitation scheme (MFE), i.e., the single frequency excitation (SFE) described in Eq. (5) is replaced by

$$E_t = \sum_{i=1}^{f_{\text{tot}}} E_i \sin(\omega_i \tau_n n_c + \varphi_i), \tag{33}$$

where f_{tot} is the total number of frequencies, E_i is the excitation bitmap for the i th frequency ω_i, and φ_i is the ith initial phase. In what follows, we set $E_i = E$, meaning a uniform frequency spectrum.

Each point in the simulation space has a complex oscillating movement resulting from the superposition of the whole set of waves of different frequencies with unknown amplitudes, and we are interested in extracting each frequency component from the multifrequency wavefield.

In order to guarantee that the waves could reach every point within the simulation space, we established the following criterion: the total number of iteration cycles n_c^{tot} should be such that it ensures that a wave can travel at least twice the longest straight distance within the simulation space. For a bitmap of $p \times q$ pixels and a wave speed v_{d0}, the minimum number of cycles is

$$n_c^{\text{tot}} = 2\frac{\sqrt{p^2 + q^2}}{v_{d0}}. \tag{34}$$

The different frequencies of each pixel are usually extracted using the numerical Fourier transform [42] of the time–domain oscillation of each point. In this section, we present an alternative method called tuning filter (TF) to extract the different frequencies from the multifrequency oscillation of each pixel. The method is based on the frequency response of the forced damped oscillator. This filter acts as a temporal mask applied on the simulation space. After the application of the TF to the time-varying multifrequency wavefield, a dynamic single-frequency wavefield can be visualized, allowing its processing to determine physical magnitudes such as reflectance and transmittance, for a given frequency.

A. Implementation

The TF is based on the tuning properties of the forced damped oscillator, governed by the well-known inhomogeneous differential equation

$$\frac{F_{\text{ext}}}{m} = \frac{d^2 z}{dt^2} + \gamma_{\text{do}} \frac{dz}{dt} + \omega_{\text{do}}^2 z, \tag{35}$$

where F_{ext} is the applied external force, z and t are the position and time variables, respectively, γ_{do} is the damping constant, and $\omega_{\text{do}} = \sqrt{k_{\text{do}}/m_{\text{do}}}$ is the natural frequency of the damped oscillator (k_{do} is the spring elastic constant and m_{do} is its mass). The TF uses the characteristic frequency response of the forced damped oscillator, which acts as a narrow band filter and maximizes the signal at resonance, i.e., when the frequency of F_{ext} equals the natural frequency ω_{do} of the oscillator. Under the condition $\gamma_{\text{do}} \ll \omega_{\text{do}}$, the bandwidth of the resonance peak is given by

$$\Delta\omega \approx \gamma_{\text{do}}, \tag{36}$$

the resonant frequency is

$$\omega_r = \sqrt{\omega_{\text{do}}^2 - \frac{\gamma_{\text{do}}^2}{2}} \approx \omega_{\text{do}}, \tag{37}$$

and the sharpness of the resonance peak is determined by the quality factor Q, defined as

$$Q = \frac{\omega_{\text{do}}}{\gamma_{\text{do}}}. \tag{38}$$

Larger Q values correspond to sharper resonance peaks.

The implementation of the TF is similar to that of the DF. The simulation space where the multifrequency wavefield is evolving is considered as the main plane. Then, a damped oscillator is associated to each point of the main plane, forming a two-dimensional array of oscillators, called the secondary plane. As schematized in Fig. 14, the wavefield amplitude at each point in the main plane is used to generate a proportional force that is applied to the particle of mass m_{do} in the corresponding oscillator. The displacement of each particle in the secondary plane is associated with the amplitude of the filtered wavefield. The oscillators are tuned at the frequency to be isolated, and then the value of ω_{do} is selected accordingly. Therefore, as many secondary planes as frequencies to be extracted will be needed.

The main advantage of the MFE is that the computing time is significantly reduced compared with the SFE. In principle, the MFE employs the same time to complete the simulation of the wavefield as that used by the SFE for just a single frequency. For a spectrum containing f_{tot} discrete frequencies, the total number of iteration cycles is reduced f_{tot} times with respect to the number of iteration cycles required to process

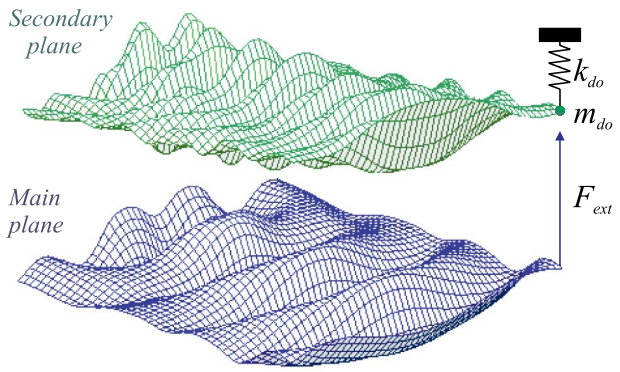

Fig. 14. Schematic diagram of the TF implementation.

the same signal when a sequential sweep of f_{tot} single frequencies is carried out. However, the advantage in speed is compensated for by a requirement of more memory to store the whole set of secondary planes and their respective auxiliary variables, which also introduces a slight delay in the computing time of each iteration cycle of the MFE compared with that of the SFE. This delay increases with the number of simultaneous frequencies explored in the MFE. More precisely, the computing times for a single iteration cycle within each excitation scheme are related by

$$t_{\text{MFE}} = t_{\text{SFE}}(1 + \delta_{\text{MFE}} f_{\text{tot}}), \tag{39}$$

where δ_{MFE} is the additional fraction of t_{SFE} required by each frequency. In the case of the algorithm implemented in this work, $\delta_{\text{MFE}} \approx 0.04$. In general, δ_{MFE} could vary according to the dynamic memory allocation efficiency of the implemented algorithm. Taking into account Eq. (39), to run a whole set of frequencies, the MFE requires less computing time than the SFE if

$$n_{cS}^{\text{tot}} > (1 + \delta_{\text{MFE}} f_{\text{tot}}) n_{cM}^{\text{tot}}, \tag{40}$$

where n_{cM}^{tot} is the total number of iteration cycles for the MFE and $n_{cS}^{\text{tot}} = f_{\text{tot}} \cdot n_c^{\text{tot}}$ is the total number of iteration cycles for the SFE.

While n_{cS}^{tot} is only determined by the size of the simulation space and by f_{tot}, in the case of the MFE, n_{cM}^{tot} is also conditioned by the required selectivity of the TF, which depends on $\Delta\omega$ and on f_{tot}. According to Eq. (36), to perform an adequate isolation of a single-frequency component, the separation between adjacent discrete frequencies should be $\Delta\omega \geq \gamma_{\text{do}}$. In addition, the TF should work under the stationary regime, i.e., when the nontuned frequency oscillations have vanished. Since the time employed by the oscillator to reach the stationary regime is inversely proportional to γ_{do}, the time required by the TF to isolate the selected frequency component basically depends on the desired resolution $\Delta\omega$. Consequently, the value of γ_{do} should be adjusted according to the speed and precision requirements of the simulation in each particular case, and this determines the value of n_{cM}^{tot}. According to the above considerations, one could decide which scheme is more appropriate.

B. Discretization Requirements and Validation

In the case of the optical spectrum ($\lambda \in [380, 780$ nm$]$) discretized in steps of 10 nm (41 frequency values), the value of n_{cM}^{tot} required for an appropriate separation of frequencies is large, since in this case $\Delta\omega$ is small, and then the required quality factor is very high [see Eqs. (36) and (38)]. Moreover, to minimize the noise produced by the nontuned components in the tuned frequency wave, it is even convenient to choose $\gamma_{\text{do}} \ll \Delta\omega$, and this implies a high value of n_{cM}^{tot}. The total number of cycles n_{cM}^{tot} required by the TF to extract a frequency component could, in principle, be reduced by increasing the time adapting constant τ_n [see Eq. (5)], i.e., by increasing ω_d. As mentioned in Section 2, the Nyquist–Shannon criterion imposes $\omega_d < \pi$. However, it was found that for high values of ω_d, the TF resonates at a frequency higher than the tuned frequency. Then, to ensure that the TF selects the desired frequency, ω_d must satisfy $\omega_d \ll \pi$, and therefore

$$v_d\sigma_p = \frac{\omega_d c}{\omega} \ll \frac{\pi c}{\omega} \tag{41}$$

for ω_d and ω being the maximum digitized and physical frequency contained within the analyzed spectrum, respectively.

In order to quantify the performance of the TF independently from other characteristics of the simulation, we define the relative error (in percentage) of the obtained intensity as a function of the explored wavelength as

$$\varepsilon_r(\lambda_e) = 100\frac{|I_{\mathrm{MFE}}(\lambda_e) - I_{\mathrm{SFE}}(\lambda_e)|}{I_{\mathrm{SFE}}(\lambda_e)|}, \tag{42}$$

where $I_{\mathrm{MFE}} = (A_M^{\max})^2$ and $I_{\mathrm{SFE}} = (A_S^{\max})^2$ are the intensities obtained with the MFE for the wavelength λ_e and the SFE, respectively, and $A_M^{\max}$ and $A_S^{\max}$ are the maximum amplitudes detected at the final stage of the time evaluation (in which the TF is in the stationary regime) for the MFE and the SFE cases, respectively.

The exploration of the optical spectrum with a resolution of 10 nm is an extreme situation for the MFE scheme because, as mentioned above, for 41 simultaneous frequencies, a very high quality factor is needed, which leads to a very large number of iteration cycles n_{cM}^{tot}. This limitation can be overcame by exploring the same amount of frequencies in several MFE stages having a larger separation between frequencies, in such a way that different frequencies are covered in each stage. In this manner, the required quality factor of the TF is greatly decreased, and therefore n_{cM}^{tot} is also considerably reduced. For example, the optical spectrum can be explored in five MFE stages with a resolution of 50 nm ($f_{\mathrm{tot}} = 9$). In this case, an error of $\varepsilon_r = 5.25\%$ can be achieved with $n_{cM}^{\mathrm{tot}} = 50,000$ cycles per stage, $\gamma_{\mathrm{do}} = 10^{-4}$ rad/cycle, $\sigma_p = 19$ nm/pixel, and $v_{d0} = 0.5$ pixels/cycle. Therefore, the total number of cycles required to explore the 41 frequencies is $5n_{cM}^{\mathrm{tot}} = 250,000$. For $\delta_{\mathrm{MFE}} \approx 0.04$, the MFE scheme becomes more suitable than the SFE in terms of computing time to explore the 41 optical frequencies, if the simulation space becomes larger than 1454×1454 pixels. This example shows that, for large simulation spaces, the MFE (and the use of the TF) represents an advantage over the SFE that can be implemented in any conventional computer. The decision on which scheme (MFE or SFE) is more suitable will in general depend on the maximum allowed error in each particular case. If we are just interested in the visualization of the field associated to each frequency, less precision is required, and in this case the whole set of frequencies can be analyzed in a single stage, with a higher value of γ_{do}, which considerably reduces the required number of iteration cycles.

As an example, the field scattered by an opaque cylinder of diameter 620 nm was simulated for an incident optical multifrequency plane wave ($\lambda \in [380, 780$ nm$]$, $\Delta\lambda = 10$ nm) with $\gamma_{\mathrm{do}} = 10^{-4}$ rad/cycle, $\sigma_p = 20$ nm/pixel, $v_{d0} = 0.5$ pixels/cycle, and a simulation space of 150×150 pixels. Figure 15(a) shows the resulting multifrequency intensity diagram for the scattered wavefield and Figs. 15(b)–15(d) are the intensity diagrams for several extracted components of wavelengths 780, 570, and 380 nm, respectively, for $n_{cM}^{\mathrm{tot}} = 600$. The white dashed line denotes the cylinder position. As can be observed, even for a very low number of iteration cycles, the TF allows a

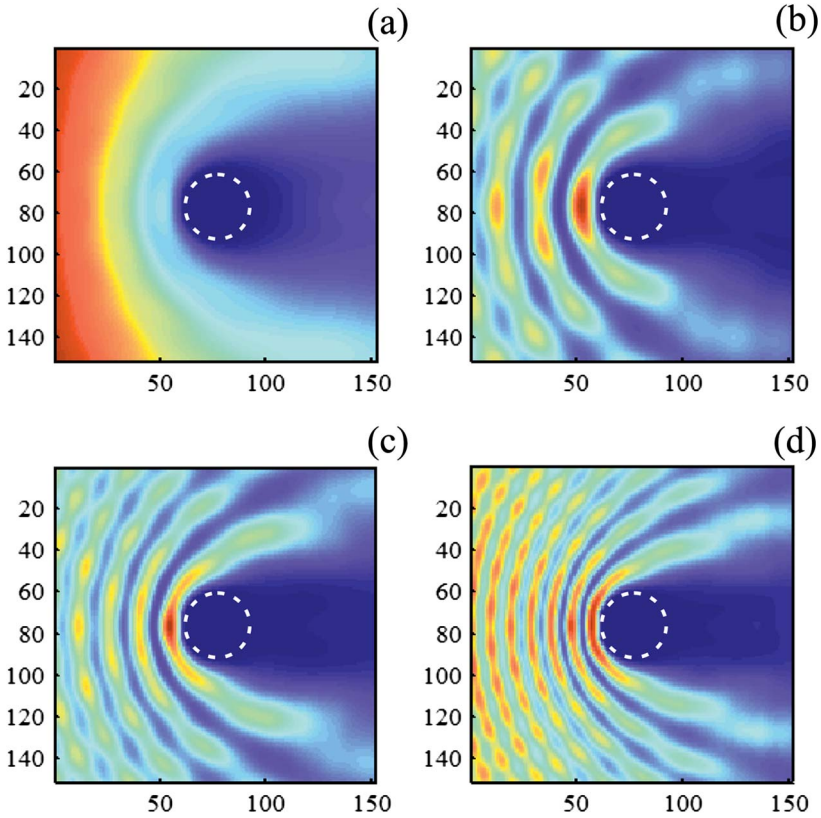

Fig. 15. Simulated intensity diagram of a multifrequency plane wave scattered by an opaque cylinder of a diameter of 620 nm. (a) The multifrequency wavefield, (b) $\lambda = 780$ nm component, (c) $\lambda = 570$ nm component, and (d) $\lambda = 380$ nm component.

clear visualization of the wavefield of each frequency. This result can be explained by taking into account that if γ_{do} is relatively high, the nontuned frequency components are rapidly damped and the filter would immediately be oscillating at its tuning frequency, although the stationary regime has not been strictly reached.

The possibility of getting a clear and rapid visualization of the selected frequency components by means of the TF could also be useful to decouple the different frequency components that coexist in a multifrequency field of mechanical waves obtained experimentally. A few thousands of frames of an experimental evolving multifrequency wavefield could be enough to decouple and visualize the evolution of a single-frequency component. This feature also makes the TF a valuable tool for visualization and signal processing of experimental data.

6. NEAR TO FAR FIELD TRANSFORMATION

The presented simulation method provides the near field distribution of a wave interacting with a given object. However, in many cases one is interested in the far field response of an illuminated structure. In this section, we show how the present simulation has been adapted to apply conventional near to far field transformation methods.

Near to far field transformation methods are usually based on Green's Theorem [28,43] and require a complex wavefield to be applied. If the wavefield is represented by a complex phasor $Z(\mathbf{r},t) = Z_R(\mathbf{r},t) + iZ_I(\mathbf{r},t)$, according to Green's theorem [28], for a fixed time we have

$$Z_t(\mathbf{r}) = \oint_{C_a} [G(\mathbf{r}|\mathbf{r}')\widehat{n}'_a \cdot \nabla' Z_t(\mathbf{r}') - Z_t(\mathbf{r}')\widehat{n}'_a \cdot \nabla' G(\mathbf{r}|\mathbf{r}')]\mathrm{d}C', \tag{43}$$

where $Z_t(\mathbf{r})$ is $Z(\mathbf{r},t)$ evaluated at a fixed t, $\mathbf{r}'$ is the position of a source point over an arbitrary contour C_a enclosing the scatterer, $\hat{n}_a$ is the outward unit normal to the contour C_a, $\mathbf{r}$ is an observation point outside C_a, and $G(\mathbf{r}|\mathbf{r}')$ is the Green's function, which in two dimensions is given by the Hankel function

$$G(\mathbf{r}|\mathbf{r}') = \frac{i}{4}H_0^{(2)}(k|\mathbf{r}-\mathbf{r}'|) \tag{44}$$

with i being the imaginary unit and $k = 2\pi/\lambda$ the wavenumber. To apply Eq. (43) and calculate the far field, we need to have the complex near field $Z_t(\mathbf{r})$ for each pixel. However, the present simulation method provides a real scalar wavefield, and then, its imaginary part should be found. Taking into account that

$$Z_{\mathbf{r}}(t) = A_{\mathbf{r}}(t)e^{-i\omega t} = A_{\mathbf{r}}(t)\cos(\omega t) - iA_{\mathbf{r}}(t)\sin(\omega t), \tag{45}$$

where $A_{\mathbf{r}}(t)$ is the amplitude of the phasor at a fixed position $\mathbf{r}$ and ω is the angular frequency in a steady state (when $A_{\mathbf{r}}(t)$ is constant), it is easily verified that

$$Z_I(\mathbf{r},t) = \frac{d}{dt}\{Z_R(\mathbf{r},t)\}. \tag{46}$$

Since the simulation provides $Z_R(\mathbf{r},t)$, we use Eq. (46) to calculate $Z_I(\mathbf{r},t)$, and therefore to build the phasor for each pixel that is introduced into Eq. (43) to calculate the far field.

In the case of a such multifrequency excitation as that described in Section 5, the far field should be calculated from the near field for each frequency component ω_i [see Eq. (33)], which is isolated from the multifrequency wavefield by means of the TF described in Section 5.

7. APPLICATION EXAMPLE

To demonstrate the potential of the improved simulation presented in this work, in this section we show an application example which includes the whole set of techniques proposed, and obtain the optical response of a highly complex biological structure. In particular, we evaluate the optical response of the peridium—a transparent protective layer that encloses the mass of spores—of the *Diachea leucopoda* (Physarales order, *Myxomycetes* class), which is a microorganism that has a characteristic pointillistic iridescent appearance [see Fig. 16(a)]. It has been demonstrated that this appearance results from a photonic effect [17]. In [44], we used a basic implementation of the present simulation method to investigate the structural color generation in this microorganism.

We use a TEM image of the peridium cross section of the *Diachea leucopoda*, shown in Fig. 16(b), to set the M bitmap, which defines the refraction index distribution by means of a linear conversion of the gray levels of the negative image of Fig. 16(b). The gray level 0 (black) is associated with the lowest value of the refraction index (equal to unity). The average refraction index of the peridium was set to 1.78, which corresponds to a common value found in biological tissues. The optical source is a Gaussian beam of width 2 μm. A total of 41 optical frequencies were explored in the range 380–780 nm with a spacing of 10 nm. The simulation space was set to be of 280×230 pixels and $\sigma_p = 15$ nm/pixel. The width of the

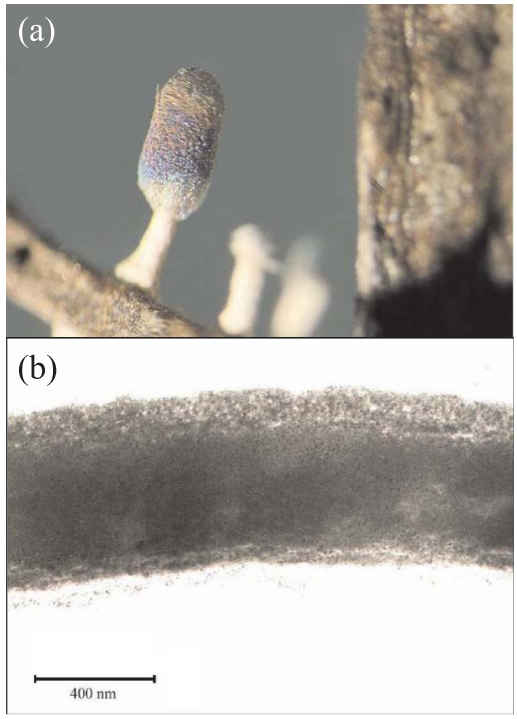

Fig. 16. (a) *Diachea leucopoda* observed under the optical microscope and (b) TEM image of the peridium cross section.

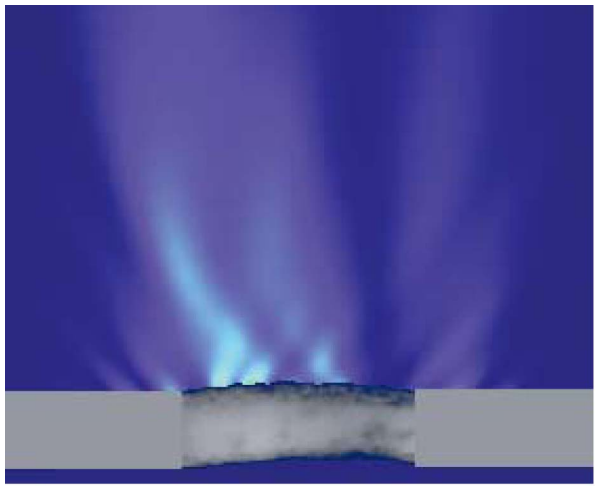

Fig. 17. Reflected near field intensity diagram produced by the peridium of the *Diachea leucopoda* obtained with the simulation method, for a wavelength of 380 nm. Brighter regions correspond to higher intensities.

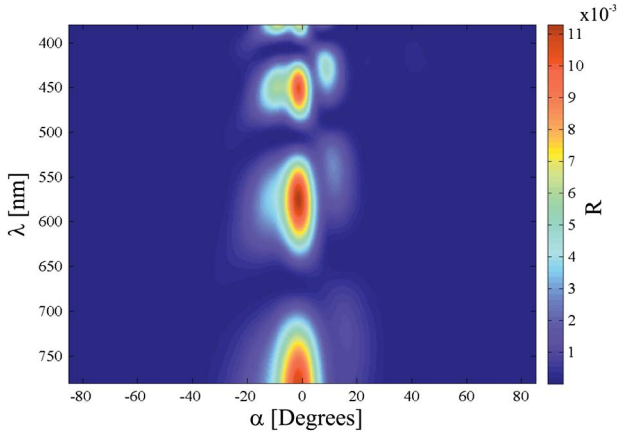

Fig. 18. Far field reflectance (R) as a function of the observation angle α and of the wavelength λ for the peridium of the *Diachea leucopoda*.

sample obtained from the TEM image is 1.68 μm and its mean thickness is 550 nm. In order to avoid errors produced by the finite size of the peridium image, we extended the biological slab at both sides by planar homogeneous slabs whose thickness is the average thickness of the actual image and whose refraction index is its average refraction index.

Figure 17 shows the resulting near field distribution of reflected intensity produced by the peridium cross section for a wavelength of 380 nm, and Fig. 18 shows the far field reflectance (R = reflected intensity/incident intensity) as a function of the observation angle α and of the wavelength λ.

8. CONCLUSION

In this paper, we presented a set of techniques to enhance the performance of a previously published electromagnetic wave simulation method from the point of view of computing time optimization and space saving. The method is suitable for dealing with dielectric objects of arbitrary shapes and refraction index distributions. The improvements introduced permit the control and analysis of the propagating waves within the simulation and results particularly suitable for investigating the electromagnetic response of biological photonic structures that usually present a high degree of complexity in their geometry as well as in the materials involved. The proposed techniques include a DF that permits decoupling waves traveling in different directions, a dynamic absorber that prevents the reflection of waves at the edges of the simulation space in order to reproduce unbounded spaces, and a TF that allows multifrequency excitation. We also adapted a near to far field method to calculate the far field with a minimum use of computation time and allocation space. As an application example, we calculated the reflectance of the transparent cover layer of a microorganism that exhibits iridescence, for multiple wavelengths and observation angles.

In its present form, the proposed simulation method computes the electromagnetic response in the case of TE (electric field perpendicular to the plane of incidence) polarized incident light. In order to fully simulate the electromagnetic response of complex structures with translational invariance, the transverse magnetic polarization mode (magnetic field perpendicular to the plane of incidence) should also be included. This would require an extension of the method to a fully vectorial formulation that is already under development. Also, we plan to make this enhanced method capable of dealing with 3D objects. As stated above, most biological structures are highly complex and require a 3D model to properly account for their electromagnetic properties. The development of such a tool would constitute a valuable contribution to the study of natural photonic structures.

ACKNOWLEDGMENTS

The authors gratefully acknowledge partial support from Consejo Nacional de Investigaciones Cientficas y Técnicas (CONICET PIP 112-200801-01880) and Universidad de Buenos Aires (UBA-20020100100533).

REFERENCES

1. V. G. Veselago, "The electrodynamics of substances with simultaneously negative values of ε and μ," Sov. Phys. Usp. **10**, 509–514 (1968).
2. J. B. Pendry, "Negative refraction makes a perfect lens," Phys. Rev. Lett. **85**, 3966–3969 (2000).
3. I. Tsukerman, "Negative refraction and the minimum lattice cell size," J. Opt. Soc. Am. B **25**, 927–936 (2008).
4. L. Jensen, Z. Lei, C. T. Chan, and P. Sheng, "Photonic band gap from a stack of positive and negative index materials," Phys. Rev. Lett. **90**, 083901 (2003).
5. A. Grbic and G. V. Eleftheriades, "Overcoming the diffraction limit with a planar left-handed transmission-line lens," Phys. Rev. Lett. **92**, 117403 (2004).
6. T. Ergin, N. Stenger, P. Brenner, J. B. Pendry, and M. Wegener, "Three-dimensional invisibility cloak at optical wavelengths," Science **328**, 337–339 (2010).
7. M. Settle, R. Engelen, M. Salib, A. Michaeli, L. Kuipers, and T. F. Krauss, "Flatband slow light in photonic crystals featuring spatial pulse compression and terahertz bandwidth," Opt. Express **15**, 219–226 (2007).
8. D. O'Brien, A. Gomez-Iglesias, M. D. Settle, A. Michaeli, M. Salib, and T. F. Krauss, "Tunable optical delay using photonic crystal heterostructure nanocavities," Phys. Rev. B **76**, 115110 (2007).
9. J. Valentine, J. Li, T. Zentgraf, G. Bartal, and X. Zhang, "An optical cloak made of dielectrics," Nat. Mater. **8**, 568–571 (2009).
10. J. Joannopoulos, R. Meade, and J. Winn, *Photonic Crystals* (Princeton University, 1995).
11. P. Russell, "Photonic crystal fibers," Science **299**, 358–362 (2003).
12. S. Huntington, J. Katsifolis, B. Gibson, J. Canning, K. Lyytikainen, J. Zagari, L. Cahill, and J. Love, "Retaining and

characterising nano-structure within tapered air-silica structured optical fibers," Opt. Express **11**, 98–104 (2003).
13. C. Martelli, J. Canning, B. Gibson, and S. Huntington, "Bend loss in structured optical fibres," Opt. Express **15**, 17639–17644 (2007).
14. P. Vukusic and J. R. Sambles, "Photonic structures in biology," Nature **424**, 852–855 (2003).
15. S. Kinoshita, *Structural Colors in the Realm of Nature* (World Scientific, 2008).
16. S. Berthier, *Iridescences, the Physical Colours of Insects* (Springer, 2007).
17. M. Inchaussandague, D. Skigin, C. Carmaran, and S. Rosenfeldt, "Structural color in myxomycetes," Opt. Express **18**, 16055–16063 (2010).
18. A. E. Luna, D. C. Skigin, M. Inchaussandague, and A. R. Alsina, "Structural color in beetles of South America," Proc. SPIE **7782**, 778205 (2010).
19. J. R. Andrewartha, J. R. Fox, and I. J. Wilson, "Resonance anomalies in the lamellar grating," Opt. Acta **26**, 69–89 (1979).
20. D. C. Skigin and R. A. Depine, "The multilayer modal method for electromagnetic scattering from surfaces with several arbitrarily shaped grooves," J. Mod. Opt. **44**, 1023–1036 (1997).
21. R. A. Depine and D. C. Skigin, "Multilayer modal method for diffraction from dielectric inhomogeneous apertures," J. Opt. Soc. Am. A **15**, 675–683 (1998).
22. M. G. Moharam and T. K. Gaylord, "Rigorous coupled-wave analysis of planar-grating diffraction," J. Opt. Soc. Am. A **71**, 811–818 (1981).
23. J. Chandezon, M. Dupuis, G. Cornet, and D. Maystre, "Multicoated gratings: a differential formalism applicable in the entire optical region," J. Opt. Soc. Am. **72**, 839–846 (1982).
24. R. A. Depine and M. E. Inchaussandague, "Corrugated diffraction gratings in uniaxial crystals," J. Opt. Soc. Am. A **11**, 173–180 (1994).
25. A. A. Maradudin, T. R. Michel, A. R. McGurn, and E. R. Méndez, "Enhanced backscattering of light from a random grating," Ann. Phys. **203**, 255–307 (1990).
26. M. Lester, D. C. Skigin, and R. A. Depine, "Blaze produced by a dual-period array of subwavelength cylinders," J. Opt. A **11**, 045705 (2009).
27. G. Schmidt and B. H. Kleemann, "Integral equation methods from grating theory to photonics: an overview and new approaches for conical diffraction," J. Mod. Opt. **58**, 407–423 (2011).
28. A. Taflove and S. C. Hagness, *Computational Electrodynamics: The Finite-Difference Time-Domain Method*, 3rd ed. (Artech, 2005).
29. K. Yee, "Numerical solution of initial boundary value problems involving Maxwell's equations in isotropic media," IEEE Trans. Antennas Propag. **14**, 302–307 (1966).
30. A. F. Oskooi, D. Roundy, M. Ibanescu, P. Bermel, J. D. Joannopoulos, and S. G. Johnson, "MEEP: a flexible free-software package for electromagnetic simulations by the FDTD method," Comput. Phys. Commun. **181**, 687–702 (2010).
31. M. Kolle, *Photonic Structures Inspired by Nature* (Springer-Verlag, 2011).
32. M. F. Su, I. El-Kady, D. A. Bader, and S. Lin, "A novel FDTD application featuring OpenMP-MPI hybrid parallelization," in *Proceedings of the 33rd International Conference on Parallel Processing (ICPP)*, Montreal, 2004, pp. 373–379.
33. A. E. Dolinko, "From Newton's second law to Huygens's principle: visualizing waves in a large array of masses joined by springs," Eur. J. Phys. **30**, 1217–1228 (2009).
34. T.-H. Pei and Y.-T. Huang, "Effective refractive index of the photonic crystal deduced from the oscillation model of the membrane," J. Opt. Soc. Am. B **29**, 2334–2338 (2012).
35. C. E. Shannon, "Communication in the presence of noise," Proc. Inst. Radio Eng. **37**, 10–21 (1949).
36. R. Courant, K. Friedrichs, and H. Lewy, "Über die partiellen Differenzengleichungen der mathematischen Physik," Math. Ann. **100**, 32–74 (1928).
37. P. J. Cobelli, A. Maurel, V. Pagneux, and P. Petitjeans, "Global measurement of water waves by Fourier transform profilometry," Exp. Fluids **46**, 1037–1047 (2009).
38. J. Berenger, "A perfectly matched layer for the absorption of electromagnetic waves," J. Comp. Physiol. **114**, 185–200 (1994).
39. B. Engquist and A. Majda, "Numerical absorbing boundary conditions for the wave equation," Commun. Pure Appl. Math **32**, 313–357 (1979).
40. R. L. Higdon, "Absorbing boundary conditions for difference approximations to the multi-dimensional wave equation," Math. Comp. **47**, 437–459 (1986).
41. R. L. Higdon, "Numerical absorbing boundary conditions for the wave equation," Math. Comp. **49**, 65–90 (1987).
42. B. Hennelly and J. T. Sheridan, "Generalizing, optimizing, and inventing numerical algorithms for the fractional Fourier, Fresnel, and linear canonical transforms," J. Opt. Soc. Am. A **22**, 917–927 (2005).
43. J. D. Jackson, *Classical Electrodynamics*, 3rd ed. (Wiley, 1998).
44. A. Dolinko, D. Skigin, M. Inchaussandague, and C. Carmaran, "Photonic simulation method applied to the study of structural color in myxomycetes," Opt. Express **20**, 15139–15148 (2012).